JOURNAL OF PROPULSION AND POWER
Vol. 13, No. 1, January–February 1997

Effect of Acoustic Perturbations on Liquid Jet Atomization

S. D. Heister,* M. W. Rutz,† and J. H. Hilbing†
Purdue University, West Lafayette, Indiana 47907

The effect of unsteady chamber characteristics on the atomization process is investigated using nonlinear free-surface models based on boundary element methods. Two separate scenarios are considered. In the first case, a liquid column is subjected to transverse oscillations from the gas phase. The second calculation addresses dynamic orifice mass flow caused by the presence of longitudinal acoustic perturbations. Results indicate that the atomization process can be strongly affected by these perturbations. As expected, the most prominent coupling occurs at driving frequencies that are at (or near) the natural frequency of oscillation of the liquid.

Nomenclature

a = orifice radius
I_m = modified Bessel function of the first kind, order m
K_m = modified Bessel function of the second kind, order m
k = wave number
n = mode number for column excitation, Eq. (5)
P = pressure
q = velocity normal to local surface
r = radial coordinate
t = time
U = velocity
We = Weber number, $\rho_g U^2 a/\sigma = \rho U^2 a/\sigma$ in Figs. 8–12
x = horizontal coordinate
y = vertical coordinate
z = axial coordinate
ε = density ratio, ρ_g/ρ
κ = surface curvature
ρ = density
σ = surface tension
ϕ = velocity potential
ω = oscillation frequency

Subscript
g = gas phase

Superscript
$\hat{}$ = perturbation quantity

Introduction

IN a liquid rocket engine (LRE) combustion chamber, the atomization process serves as a precursor to complex vaporization, mixing, and reaction processes. Not only is the atomization process important to characterizing the steady-state performance of an LRE, but it also can play an important role in unsteady processes within the combustion chamber. In fact, numerous authors[1–5] have implicated the atomization process as a mechanism to (at least partially) explain high-frequency LRE combustion instabilities.

Even under steady conditions, our knowledge of the detailed processes leading to atomization of a liquid jet is quite modest. For this reason, there have been relatively few efforts aimed at improving our understanding of injection processes under dynamic conditions. Most previous efforts have been experimental in nature and have been motivated by LRE combustion stability concerns.

One group of experiments has focused on longitudinal acoustic fields,[6–9] investigating both low-injection velocities[6,7] and high-injection velocities[8,9] characteristic of actual LRE injectors. These authors concluded that the presence of a time-dependent pressure field at the injection point leads to a dynamic orifice mass flow, even in the event that the injector manifold pressure remains constant. At low-injection velocities, this effect leads to periodic bulges in the jet diameter; this character also persists into the higher jet velocity regime.[6] In addition, droplet coalescence was effected by the time-dependent injection flow rate. Similar effects have been observed[10,11] when the chamber pressure is held fixed, but the flow rate is varied using piezoelectric drivers upstream of the orifice inlet. At high-injection velocities, Ingebo[9] showed a dramatic decrease in mean droplet size with the amplitude of the disturbance. This compelling evidence indicates the importance of the acoustic interaction with the atomization process.

A second group of researchers[5,12–14] has focused on interactions of a liquid jet with a transverse acoustic perturbation. Here, experiments have revealed a broadening of the jet cross section,[14] and a physical deflection of the jet caused by the crosswind from the acoustic field.[13] Here, the variable mass flow effect can also be present because the injector manifold reacts to the average pressure at the injector face and distributes fluid spatially in accordance with the local injector face pressure.[12]

Analytic models aimed at quantifying the phenomena just described have made heavy use of experimental results. Early efforts[5–7] made use of one-dimensional mass and momentum balances in which liquid and gas phases were decoupled. Other researchers have simply sought to correlate their experimental results with injection and acoustic wave conditions. More recently, the jet broadening phenomena present under some transverse acoustic interactions was quantified using a static equilibrium analysis.[14]

While these efforts have advanced our understanding of these processes, the effect of coupling of gas and liquid flowfields in a dynamic environment has yet to be considered. Recent developments of numerical models based on the use of boundary element methods (BEMs)[15,16] permit us to analyze the acoustically driven interactions previously described. The use of the BEM approach provides high resolution of the interface (under very large distortions), as well as the capability to extend simulations beyond atomization events. This article will present simulations of both longitudinal and transverse acoustic wave interactions with an initially cylindrical column

---

Presented as Paper 95-2425 at the AIAA/ASME/SAE/ASEE 31st Joint Propulsion Conference and Exhibit, San Diego, CA, July 10–12, 1995; received July 24, 1995; revision received May 30, 1996; accepted for publication June 12, 1996.

*Associate Professor, School of Aeronautics and Astronautics. Member AIAA.

†Graduate Research Assistant, School of Aeronautics and Astronautics. Member AIAA.

of fluid. Transverse simulations will include the coupling of gas and liquid velocity fields, and longitudinal simulations will include the effect of dynamic orifice mass flow in time-accurate calculations valid for nonlinear deformations of the liquid.

Classification of Acoustically Driven Instabilities

Before performing the numerical simulations described earlier, it is prudent to determine the applicable flow regimes in LREs, as well as those studied by other researchers. One important consideration involves the frequency response of the liquid to the imposed oscillation. Consider the cylindrical column of liquid subject to either longitudinal or transverse acoustic perturbations as shown in Fig. 1. Variables shown in this figure are defined in the Nomenclature.

For the transverse oscillation in Fig. 1, fundamental frequencies are obtained from a linearized, inviscid, two-dimensional analysis similar to the classic axisymmetric analysis used by Lamb[17] in the case of a droplet. In the two-dimensional case, it is straightforward to show that velocity potentials satisfying Laplace's equation in the liquid and gas phases can be represented

$$\phi = (\hat{a}\omega/n)(r/a)^n \cos(n\theta)\cos(\omega t) \tag{1}$$

$$\phi_g = -(\hat{a}\omega/n)(a/r)^n \cos(n\theta)\cos(\omega t) \tag{2}$$

assuming a surface shape $r = a + \hat{a}\cos(n\theta)\sin(\omega t)$. Here, n is the order of the oscillation, and we will assume that $\hat{a}$ is a perturbation ($\hat{a} << a$). Since the column is initially at rest, the linearized result from Bernoulli's equation can be expressed

$$P - P_g = \frac{\sigma}{a} - \rho\frac{\partial\phi}{\partial t} + \rho_g\frac{\partial\phi_g}{\partial t} = \kappa\sigma \tag{3}$$

where κ is the linearized curvature of the distorted surface:

$$\kappa = (1/a)[1 - (\hat{a}/a)(1 - n^2)\cos(n\theta)\sin(\omega t)] \tag{4}$$

Combining Eqs. (1–4), we obtain the fundamental frequencies of oscillation of the column:

$$\omega^2 = \frac{n(n^2 - 1)\sigma}{(\rho + \rho_g)a^3} \tag{5}$$

As in the case of a droplet,[17] we see that the lowest order mode is for $n = 2$. In this case, the fundamental frequency is given by $\omega^2 = 6\sigma/[(\rho + \rho_g)a^3]$, which gives a result 13% lower than that of a droplet in a low-density gas.

For the case of a longitudinal excitation, the fundamental frequency of the liquid column can be determined by analysis of a dispersion relation,[18] which describes the variation of ω with changes in k:

$$\omega^2\left[\frac{I_0(k)}{\varepsilon I_1(k)} + \frac{K_0(k)}{K_1(k)}\right] + 2ik\omega - k^2\frac{K_0(k)}{K_1(k)} - \frac{k(1 - k^2)}{We} = 0 \tag{6}$$

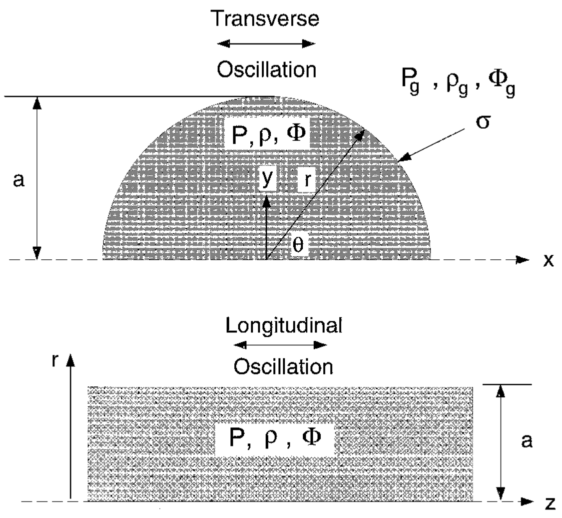

Fig. 1 Liquid jets subjected to transverse and longitudinal acoustic oscillations.

Here, we assume that variables have been nondimensionalized using the jet radius, jet velocity, and liquid density as dimensions. Under this assumption, $\varepsilon = \rho_g/\rho$ and $We = \rho_g U^2 a/\sigma$ are the relevant dimensionless groups. Equation (6) is developed assuming a jet deformation of the form

$$r = 1 + (\hat{a}/a)e^{\omega t + ikz} \tag{7}$$

such that the real part of ω corresponds to the growth rate of disturbances with k and the imaginary part of ω represents the characteristic frequency of disturbances traveling along the surface. Following Sterling and Sleicher,[18] we presume that after some finite time, only the disturbance with maximum growth rate will be present. By iterating on various k values, we can find the wave number of the disturbance satisfying this criteria and determine the fundamental frequency response (imaginary part of ω) corresponding to this condition.

Using these notions, we can characterize the frequency and flow regimes investigated by various researchers, as well as those present in engines that have experienced combustion instabilities. Data resulting from this procedure are summarized in Table 1. This table summarizes experimental results from cold flow[4,6,14] and combusting[9,19] flows with imposed oscillations. Ingebo[9] ran a series of combusting experiments under oscillating chamber pressure conditions (created using a siren at the chamber exit), while Oefelein and Yang[19] report on the extensive data available from stability testing of the F-1 engine. This engine exhibited tangential-mode instabilities in many of the early injector designs. In the case of transverse oscillations, Weber numbers in Table 1 are based on estimated peak crossflow velocities, and liquid frequencies are calculated using the primary ($n = 2$) mode in Eq. (5). For longitudinal oscillations, Weber numbers are based on jet velocity, and ω values are calculated from Eq. (6).

Results indicate that frequencies observed in firings (or utilized in tests) are within (or near) the natural frequency range

Table 1 Frequency characterization, acoustic interactions

				Frequencies in hertz	
Researcher(s)	$\Delta P/P$	$\varepsilon x10^3$	We	ω_g	ω
Reba and Brosilow[6] (L)	0.03–0.49	1.2–4.2	0.38–21	250–500	4–2,700
Ingebo[9] (L)	0.11–0.22	0.5–4.4	47–1,700	1,190	600–373,000
Miesse[4] (T)	——	1.2	——	1,100–8,800	100–400
Hoover et al.[14] (T)	0.0046–0.055	1.2–14	0.03–80	500–2,500	470–920
Oefelein and Yang[19] (T)	0.65–4.0	17.8	——	454–538	80–270[a]

Note: (T) and (L) denote tangential and longitudinal modes, respectively.
[a]Fuel and oxidizer orifices for 5*U* and double-row cluster injectors.

of the liquid columns. In particular, the observed instability frequencies in the F-1 engine are very near the natural frequency of oscillation for fuel jets used in early (unstable) injector designs for this engine. Since $\omega \propto a^{-1.5}$, the natural frequency of the column doubles with a 37% reduction in jet radius (presumed to occur with the shedding of drops from the periphery). Therefore, it will be fruitful to investigate jet response near the condition $\omega \approx \omega_g$ to investigate coupling between the atomization process and the acoustic modes from the chamber.

Modeling Approach

Liquid jet atomization problems represent significant challenges to modelers because of the nonlinear nature of the free surface, and viscous and turbulence effects. Current models are unable to address all of these physical processes. The present analysis is intended to shed some light on the gross response of liquid jets to both longitudinal and transverse acoustic oscillations. In particular, we will presume that both liquid and gas phases are incompressible and inviscid with negligible turbulence in the flow. The lack of viscosity in the gas implies that pressure distributions in separated regions will not be resolved. In the liquid, viscosity does not alter the basic surface shape unless droplet sizes are of the same order as the boundary-layer thickness.

Many authors have proposed that the gas field can be treated as locally incompressible in analyzing the flow of the gas around the liquid jet. This assumption is valid when the wavelength of the acoustic disturbance is much larger than that which is applicable to the liquid. In our case, wavelengths in the gas phase are proportional to combustion chamber dimensions, whereas the wavelength in the liquid jet is proportional to the orifice size. Since the orifice is typically 2–3 orders of magnitude smaller than the applicable chamber dimension, the incompressible gas phase assumption is prudent.

In this section, we will choose the jet radius a, liquid density ρ, and a characteristic velocity U as dimensions. Under this nondimensionalization, $We = \rho_g U^2 a/\sigma$ and the gas/liquid density ratio $\varepsilon = \rho_g/\rho$ are the two dimensionless variables characterizing these flows. For an inviscid gas or liquid domain, velocity potentials ϕ_g and ϕ exist, and must satisfy Laplace's equation:

$$\nabla^2\phi = \nabla^2\phi_g = 0 \tag{8}$$

The unsteady Bernoulli equation provides conditions relating velocity potentials at the gas/liquid interface

$$\frac{\partial\phi}{\partial t} + \frac{1}{2}(\nabla\phi)^2 + P_g + \frac{\kappa}{We} = 0 \tag{9}$$

where P_g is the dimensionless gas pressure at the interface, and κ is the local surface curvature. On the gas side of the interface, Bernoulli's equation is

$$\varepsilon\frac{\partial\phi_g}{\partial t} + \frac{\varepsilon}{2}(\nabla\phi_g)^2 + P_g = 0 \tag{10}$$

Mathematically, Eqs. (8–10) provide a well-posed set of equations for velocity potentials, the gas pressure at the interface, and the shape of the interface (implicit in κ). This set of equations is solved using a BEM, which begins with an integral representation of Laplace's equation:

$$\alpha\phi(\boldsymbol{r}_i) + \int_\Gamma\left(\phi\frac{\partial G}{\partial n} - qG\right)\mathrm{d}\Gamma = 0 \tag{11}$$

where $\phi(\boldsymbol{r}_i)$ is the value of the potential at a point $\boldsymbol{r}_i$, Γ denotes the boundary of the domain, and G is the free-space Green's function corresponding to Laplace's equation. An analogous form of Eq. (11) can also be derived for the gas phase potential. For a well-posed problem, either ϕ or $q = \partial\phi/\partial n$ must be specified at each node on the boundary. Here, n is the unit vector pointed outward from the boundary, so that q represents the velocity normal to the boundary. The quantity α in Eq. (11) results from singularities introduced as the integration passes over the boundary point $\boldsymbol{r}_i$.

Using this methodology, models have been developed for both two-dimensional[20] and axisymmetric[15] flowfields. If we let r and z denote radial and axial coordinates, respectively, and denote the base point with subscript i, the Green's function solution to the axisymmetric Laplacian can be written

$$G = \frac{4rK_e(p)}{\sqrt{(r + r_i)^2 + (z - z_i)^2}} \tag{12}$$

where

$$p = \frac{(r - r_i)^2 + (z - z_i)^2}{(r + r_i)^2 + (z - z_i)^2} \tag{13}$$

and $K_e(p)$ is the complete elliptic integral of the first kind. For computational efficiency, this quantity is calculated using a curve fit,[15] which has an accuracy to 10^{-8}.

In the case of a two-dimensional flow (letting x and y represent the coordinates), we have

$$G = (1/2\pi)\ell n|\boldsymbol{r} - \boldsymbol{r}_i| = (1/4\pi)\ell n[(x - x_i)^2 + (y + y_i)^2] \tag{14}$$

In both cases, we presume that both ϕ and q vary linearly along the length of a given element. This assumption permits the construction of a set of matrices involving the nodal values of ϕ and q and the integrals (over a given element) given in Eq. (11). For the two-dimensional flows, integration across a segment can be carried out analytically. Singularities resulting from integration across a segment containing the base point are also integrable.[20] In the case of axisymmetric flow, the integrations must be carried out numerically.[15] In this case, we choose a four-point Gaussian quadrature for evaluation of integrals. Logarithmic singularities that arise in the elliptic integral when the segment contains the base point are treated with a special Gaussian integration designed to accurately treat this condition.

Nodes on the interface are assumed to travel with the local liquid surface velocity, and so a transformation from the Eulerian to Lagrangian reference frame is required. After this transformation, Eqs. (9) and (10) become

$$\frac{\mathrm{D}\phi}{\mathrm{D}t} = \frac{1}{2}(\nabla\phi)^2 - P_g - \frac{\kappa}{We} \tag{15}$$

$$P_g = -\frac{\varepsilon}{2}(\nabla\phi_g)^2 - \varepsilon\frac{\mathrm{D}\phi_g}{\mathrm{D}t} + \varepsilon\nabla\phi\cdot\nabla\phi_g \tag{16}$$

In these expressions, the notation $\mathrm{D}/\mathrm{D}t$ denotes changes in time for nodes moving with the liquid interfacial velocity.

Surface slope and curvature are obtained from a fourth-order treatment to ensure accurate resolution of the surface. Cubic splines are used to fit current locations of surface nodes for the purpose of regridding as the calculation proceeds. Regridding is necessary in many calculations because of the tendency of nodes to bunch in regions of highest curvature. Models have been validated (for nonlinear calculations) to ensure that solutions are insensitive to the grid that has been selected. Droplets are assumed to be pinched from the main body of fluid if a node lies within 5% of the orifice radius of the centerline (or another node). Numerous validations have proven that solutions are insensitive to this pinch criterion. Using this methodology, the BEM formulation permits accurate solution of highly distorted interfaces in an unsteady flow.

Computational Grids and Boundary Conditions

Transverse Mode Simulations

Figure 2 highlights the computational grid and boundary conditions employed for coupled, two-dimensional simulations of a liquid column subjected to an acoustic oscillation. For this problem, We, ε, and the gas/liquid frequency ratio ω_g/ω are input parameters for a given simulation. Assuming quantities are nondimensionalized using the liquid density, column radius, and peak acoustic velocity, the dimensionless liquid column natural frequencies [Eq. (5)] can be written

$$\omega^2 = \frac{\varepsilon n(n^2 - 1)}{(1 + \varepsilon)We} \qquad (17)$$

We presume that the acoustic oscillation can be represented by a simple sine wave, so that the gas-phase velocity potential far from the column may be written

$$\phi_g = x \sin(\omega_g t/2) \qquad (18)$$

The factor of $\frac{1}{2}$ is included inside the sine function to account for the fact that the inviscid solution is insensitive to the direction of gas flow. Numerical experiments indicate that far-field conditions may be accurately assumed if the outer gas boundary is placed 15 jet radii from the origin.

For nodes along the symmetry axis in Fig. 2, the q is assumed to be zero, while the Bernoulli conditions [Eqs. (15) and (16)] provide the necessary boundary information for liquid and gas nodes lying on the free-surface boundary. A stable, accurate, treatment of the coupling of the two flows through the gas pressure [which appears in both Eqs. (15) and (16)], has been developed.[15,20] The treatment begins by solving for liquid surface velocities from Eq. (11) and noting that $q_g = -q$ on the surface, since we are tracking nodes with respect to the motion of the liquid. Given the q_g value on the surface, solution of the analogous form of Eq. (11) provides current values for ϕ_g on the interface. The current gas pressure is then computed from Eq. (16) by approximating the $D\phi_g/Dt$ term using a first-order backward difference. Finally, new values of ϕ on the interface (for the next time step) are obtained via integration of Eq. (15). Simulations presented in the following section employ 17–33 nodes along the interface, and typically run in a few hours on a Sun Sparcstation 5 using a dimensionless time step of 0.005.

Longitudinal-Mode Simulations

Longitudinal-mode simulations are performed by assuming that an oscillation in chamber pressure at the injector face will lead to a dynamic mass flow through the orifice. Under this assumption, we employ the axisymmetric model of Hilbing et al.,[15] with an unsteady inflow as indicated in Fig. 3. For this calculation, the presence of the gas is neglected, and nodes placed along the orifice exit plane are held fixed. Along this inflow boundary, the velocity is assumed to be

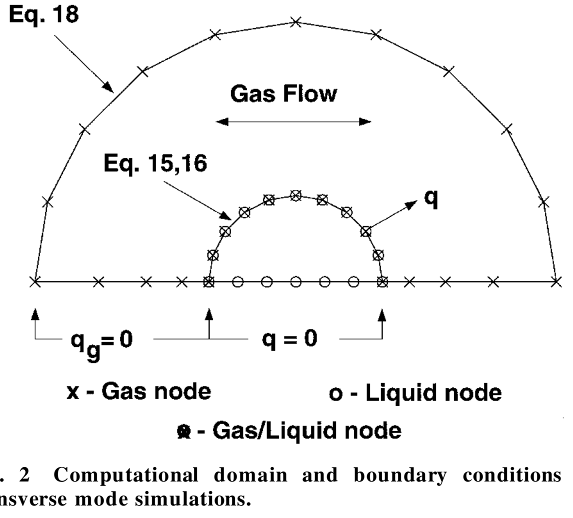

Fig. 2 Computational domain and boundary conditions for transverse mode simulations.

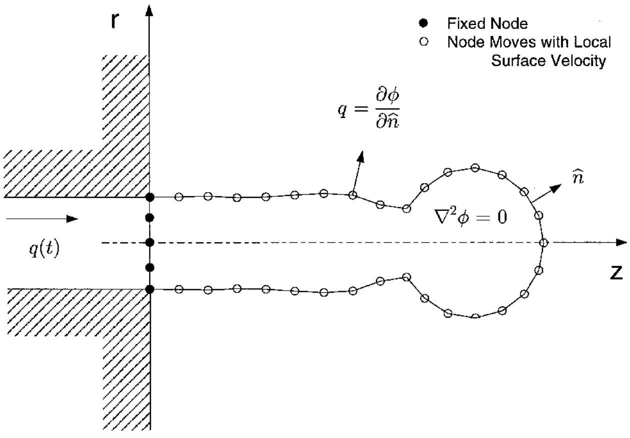

Fig. 3 Computational domain and boundary conditions for longitudinal mode simulations.

$$q = 1 + q' \sin(\omega_g t) \qquad (19)$$

where q' is the fractional change (in magnitude) of the velocity caused by pressure oscillations at the injector face. The oscillation is assumed to be at a frequency identical to that of the acoustic disturbance, and velocities are nondimensionalized against the mean velocity exiting the orifice.

For nodes lying on the free surface, Eq. (11) (with $P_g = 0$) is integrated in time to give ϕ values along the interface that serve as boundary conditions. Gravity is neglected in the simulations since its influence is very small for high-speed jets. Typical solutions employ a grid spacing corresponding to 20% of the orifice radius. Run times can vary substantially (from a few hours to several days), depending on the length of the jet, i.e., long jets have a large number of nodes and require more calculations per time step.

Results

Transverse Mode Simulations

For all simulations presented here, a gas/liquid density ratio of $\varepsilon = 0.01$ has been assumed. This value is typical of high-pressure combustion conditions, as can be noted in Table 1. Parametric studies involving this parameter[20] indicate that jet behavior is not terribly sensitive to ε for low-density ratios.

Under this assumption, the response of a column to an acoustic oscillation at the lowest-order natural frequency of the jet ($\omega_g = \omega|_{n=2}$) is shown in Fig. 4 for a Weber number of 0.1. As expected, we see a strong response under these conditions, with the distortion increasing with each successive period of the oscillation. However, for long times (several periods), a very interesting behavior results. This behavior is best observed by plotting the time history of the position of a node on the top of the column, as shown in Fig. 5. We note that the overall magnitude of the distortion is bounded, even though there is no dissipation in this inviscid simulation.

The explanation for this phenomena lies in the nonlinear behavior of the column itself. For finite deformations, the natural frequency of oscillation is reduced from that predicted by linear theory. This effect is well documented for oscillations of liquid droplets, but has not been investigated substantially for liquid columns. Figure 6 shows the nonlinear frequency shift as a function of initial surface deflection for both droplets and columns. As the jet distorts because of excitation at its

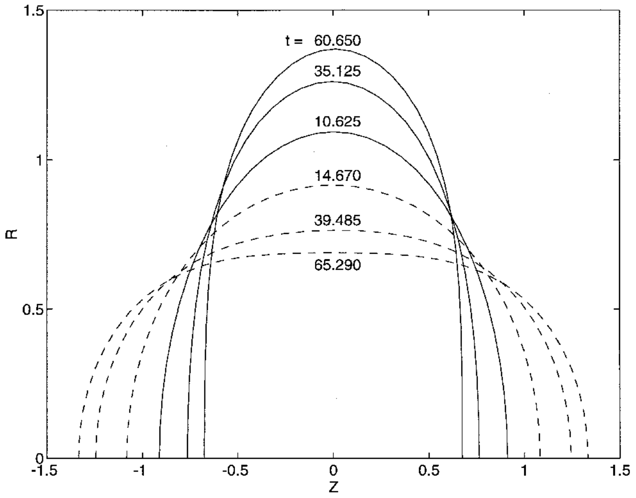

Fig. 4 Column shapes at various times of an acoustic perturbation, $\omega_g = \omega$, $We = 0.1$, and $\varepsilon = 0.01$.

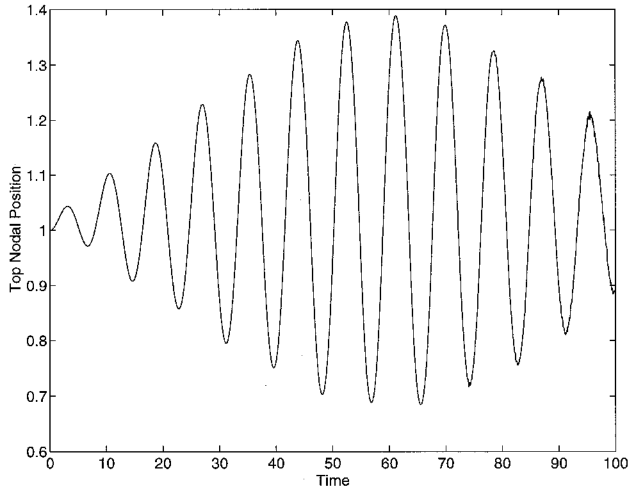

Fig. 5 Motion of a node on the top of the column during acoustic perturbation, $\omega_g = \omega$, $We = 0.1$, and $\varepsilon = 0.01$.

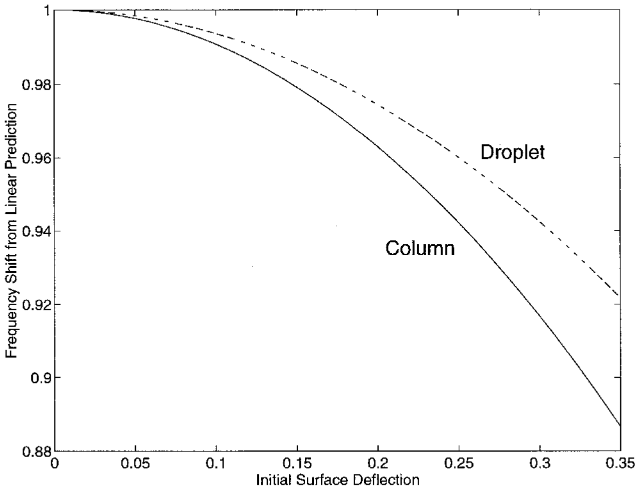

Fig. 6 Nonlinear frequency shift for liquid drops and columns under vacuum (or low gas density) conditions.

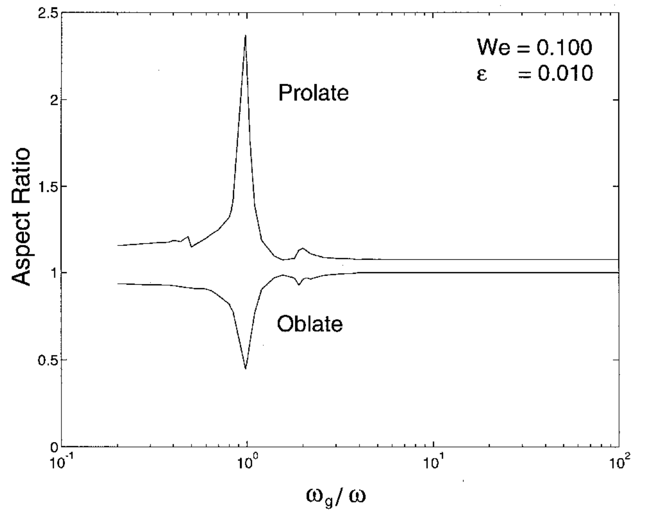

Fig. 7 Nonlinear frequency response of liquid column; maximum (prolate) and minimum (oblate) aspect ratios obtained during oscillation.

linear natural frequency, further excitation at this frequency will actually become destructive for some level of column deformation. Beyond this point, the oscillation will decay (as shown in Fig. 5) until the cycle repeats.

The overall frequency response of the column is shown in Fig. 7. As expected, we see a strong peak at excitation frequencies near the natural harmonic ($n = 2$) frequency of the column. However, it is quite interesting to note that very little response is obtained for all other frequencies in the domain. There is a small peak at the subharmonic $\omega_g = \omega_{\text{Nat}}/2$, but there is very little activity at the higher order (fourth, sixth, etc.). We expect very little response if $\omega_g >> \omega$, since the jet inertia does not permit reactions on this short time scale. In the other limit $\omega_g << \omega$, the column response is nearly quasisteady and peak deflections are simply a function of We. Note that at this condition ($We = 0.1$) very little jet broadening would be predicted for a steady crossflow as indicated in the far left-half of the curves in Fig. 7.

These results have obvious implications to LRE combustion instability. A design that has transverse acoustic modes near the jet natural frequency [$n = 2$ in Eq. (6)] will be subject to coupling from the wave structures present in the gas domain. If the jet broadens substantially, its drag will increase and it will be more subject to deflection by the transverse flow. For impinging element designs, the broadening will have direct consequences on the atomization/mixing in the impingement region. As indicated in Table 1, the F-1 injector natural frequencies do lie near the range of tangential acoustic frequencies experienced during testing of this engine. Therefore, this phenomenom could explain (at least in part) the tangential stability problems encountered by this engine. The good news is that this phenomenom appears to be limited to the lowest-order natural frequency of the column; subharmonics and higher harmonics do not play a substantial role as indicated in Fig. 7.

Longitudinal Mode Simulations

Currently, simulation of a three-dimensional, viscous, turbulent, two-phase flow that corresponds to real world conditions is well beyond current modeling capabilities. For this reason, the longitudinal simulations have been limited to a relatively low-velocity regime in which the assumptions of axisymmetry and inviscid flow are most appropriate. The main focus of these simulations is to address the effects of unsteady perturbations on the character of breakup under these assumptions. Since the simulations in this section do not include the influence of gas-phase pressure variations about the jet, the Weber number is defined in terms of the liquid density. A Weber number of 100 is assumed for results presented herein.

Figures 8 and 9 address the effect of the disturbance magnitude on the atomization process for a disturbance at the jet natural frequency. In this case, analysis of Eq. (6) indicates

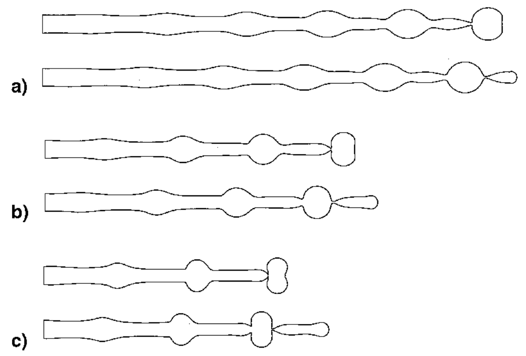

Fig. 8 Effect of longitudinal disturbance amplitude on behavior of liquid jet at *We* = 100, $\omega_g = \omega = 0.7$. q' = a) 2, b) 4, and c) 6%.

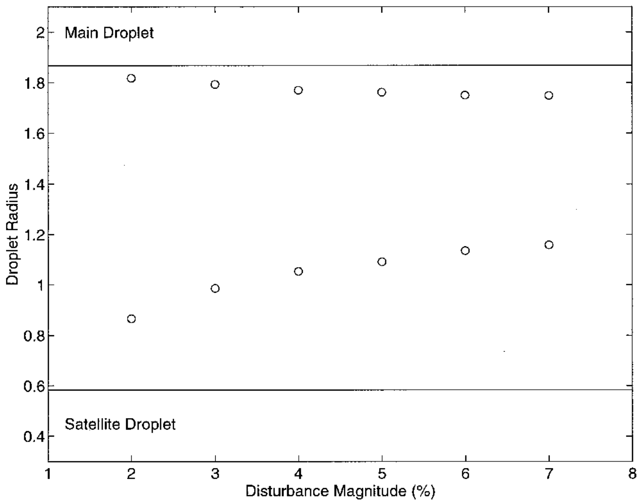

Fig. 9 Effect of longitudinal disturbance amplitude on drop size for *We* = 100, $\omega_g = \omega = 0.7$. Solid lines are for infinitesimal ($q' \approx 0$) disturbance.

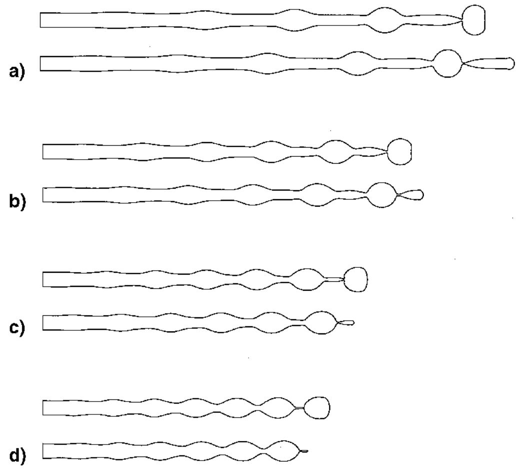

Fig. 10 Effect of longitudinal disturbance frequency on behavior of liquid jet at *We* = 100, q' = 2%. ω/ω_g = a) 0.71, b) 1.0, c) 1.29, and d) 1.57.

that a dimensionless frequency of $\omega \approx 0.7$ generates waves of the most unstable length. In Fig. 8, one can note that nonlinear effects lead to the formation of a main and satellite droplet from a single wavelength of the instability. This behavior is well known for low-speed jets. Periodic bulges appear in the jet because of the unsteady inflow, as noted experimentally by Reba and Brosilow.[6]

Increasing the size of the perturbation not only decreases jet breakup length, but also affects the shape and size of both main and satellite drops. As q' is increased, main droplets take on a squashed shape as a result of high-velocity fluid [when $\sin(\omega t) > 0$], encountering lower velocity fluid that has already exited the nozzle. This phenomena, known as the Klystron effect, has been documented qualitatively by numerous researchers.[1,8,19] Quantitative comparisons of droplet sizes are compared with an infinitesimal disturbance[16] in Fig. 9. Note that the inviscid predictions match experiments quite well in this regime. Viscosity tends to slow down the breakup process, but does not fundamentally change droplet sizes in this flow regime. The satellite size is shown to increase with perturbation amplitude at the frequency ratio selected for these simulations. Extrapolation to higher q' values would presumably lead to a monodisperse case in which both drops are the same size. Through the use of piezoelectric drivers, droplet trains of this type have been created experimentally.[10]

Figures 10 and 11 address the effect of disturbance frequency on the character of the jet. As in the case of amplitude dependence (Figs. 8 and 9), the jet behavior is also frequency dependent. In this case, increasing disturbance frequency tends to decrease breakup length even beyond $\omega_g/\omega > 1$; a trend not predicted by linear theory. In addition, the size of satellite drops tends to decrease with increasing frequency as shown in

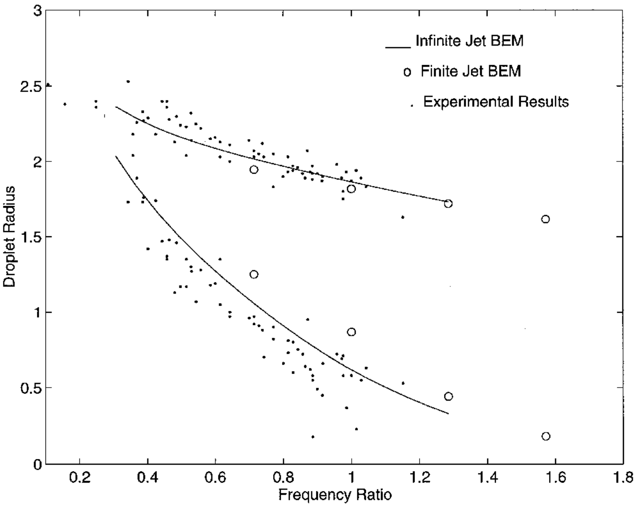

Fig. 11 Effect of longitudinal disturbance frequency on drop size for liquid jet at *We* = 100, q' = 2%. Solid lines are for $q' \approx 0$.

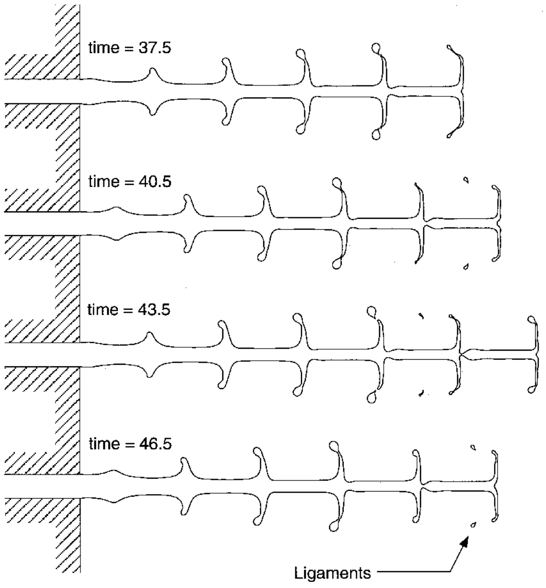

Fig. 12 Jet behavior under violent oscillation, *We* = 1000, *k* = 1, and q' = 10%.

Fig. 10. At a frequency ratio of 1.57, satellite drops have nearly vanished, indicating that a frequency near this value can produce monodisperse atomization. In fact, viscous effects would probably preclude the formation of this very small structure. Quantitative predictions of droplet sizes are shown in Fig. 11. Here, the solid lines reflect results for an infinitesimal perturbation, as in Fig. 9, and the data points are measurements of Rutland and Jameson[21] and Lafrance.[22]

A final simulation was conducted for the case of a high Weber number ($We = 1000$), large amplitude ($q' = 10\%$), perturbation. A time sequence for this case is shown in Fig. 12. In this case, the Klystron effect leads to a large radial broadening of the jet, as observed in numerous experiments.[1,8,23] Large perturbations of this nature have obvious repercussions to jet behavior, causing clustered clumps of fluid at locations corresponding to peak flow rates during the unsteady process. In addition, the droplets formed from the annular rings of fluid shown in Fig. 12 will be much smaller than drops formed from a steady atomization process; an effect observed by Ingebo.[9] Additional modeling efforts will be required to obtain a more quantitative evaluation of this effect.

Conclusions

Nonlinear two-dimensional and axisymmetric numerical simulations have been applied to simulate the effect of acoustic perturbations on liquid jet atomization processes. A liquid column is shown to react very strongly to perturbations at its lowest-order natural frequency $\omega = \sqrt{(6\sigma)/[(\rho + \rho_g)a^3]}$, but has minimal unsteady response for frequencies not near this value. Early (unstable) fuel injector designs used in the F-1 engine program were shown to be near this natural frequency. In addition, nonlinear natural frequencies for columns under finite deformation have been quantified. The frequency shift associated with a finite amplitude deformation is shown to cause a limiting amplitude of column distortion.

The response of a liquid jet to longitudinal excitation (as modeled through the use of a dynamic orifice mass flow) has also been quantified. Periodic bulges in the jet's surface, typically referred to as the Klystron effect, are described quantitatively using this model. For low-speed jets, increasing both amplitude and frequency of the disturbance is shown to increase the size of satellite drops formed by nonlinear deformation of the column. At large excitation amplitude, distinct mushroom-shaped structures appear, as described by several researchers. It is obvious that the formation of these structures will decrease mean drop size, but more effort is required to quantify the extent of the size change.

Acknowledgment

The authors gratefully acknowledge the support of this work by the U.S. Air Force Office of Scientific Research under Contract F49620-94-1-0151, under the Project Management of Mitat Birkan.

References

[1] Harrje, D. T., and Reardon, F. H. (eds.), "Liquid Propellant Rocket Combustion Instability," NASA SP-194, 1972.

[2] Jensen, R. (ed.), "JANNAF Subcommittee on Combustion Stability—Annual Report," 27th JANNAF Combustion Meeting, Cheyenne, WY, 1990.

[3] Huynh, C., Ghafourian, A., Mahalingam, S., and Daily, J. W., "Combustion Design for Atomization Study in Liquid Rocket Engine," AIAA Paper 92-0465, July 1992.

[4] Miesse, C. C., "The Effect of Ambient Pressure Oscillations on the Disintegration and Dispersion of a Liquid Jet," *Jet Propulsion*, Vol. 25, No. 3, 1955, pp. 525–534.

[5] Miesse, C. C., "Correlation of Experimental Data on the Disintegration of Liquid Jets," *Industrial and Engineering Chemistry*, Vol. 47, No. 9, 1955, pp. 1690–1701.

[6] Reba, I., and Brosilow, C., "Combustion Instability: Liquid Stream and Droplet Behavior," Polytechnic Inst. of Brooklyn, Wright Air Development Center, TR 59-720, Sept. 1960.

[7] Torda, T. P., and Schmidt, L. A., "One Dimensional Unsteady Aerothermo-Chemical Analysis of Combustion Instability in Liquid Rocket Engines," *Pyrodynamics*, Vol. 1, No. 1, 1964, pp. 89–111.

[8] Dunne, B., and Cassen, B., "Velocity Discontinuity Instability of a Liquid Jet," *Journal of Applied Physics*, Vol. 27, No. 6, 1956, pp. 577–582.

[9] Ingebo, R. D., "Atomization of Ethanol Jets in a Combustor with Oscillatory Combustion-Gas Flow," NASA TN D-3513, 1966.

[10] Dressler, J. L., "Characterization of a Velocity-Modulation Atomizer," *Review of Scientific Instruments*, Vol. 65, No. 11, 1994, pp. 3563–3569.

[11] Orme, M., "On the Genesis of Droplet Stream Microspeed Dispersions," *Physics of Fluids*, Vol. 3, No. 12, 1991, pp. 2936–2947.

[12] Heidmann, M. F., "Oxygen-Jet Behavior During Combustion Instability in a Two-Dimensional Combustor," NASA TN D-2725, Nov. 1965.

[13] Buffum, F. G., and Williams, F. A., "The Response of a Turbulent Jet to Transverse Acoustic Fields," *Proceedings of the 1967 Heat Transfer and Fluid Mechanics Institute*, Stanford Univ. Press, Stanford, CA, 1967, pp. 247–276.

[14] Hoover, D. V., Ryan, H. M., Pal, S., Merkle, C. L., Jacobs, H. R., and Santoro, R. J., "Pressure Oscillation Effects on Jet Breakup," *Heat and Mass Transfer in Spray Systems*, American Society of Mechanical Engineers, HTD-Vol. 187, New York, 1991, pp. 27–36.

[15] Hilbing, J. H., Heister, S. D., and Spangler, C. A., "A Boundary Element Method for Atomization of a Finite Liquid Jet," *Atomization and Sprays*, Vol. 5, No. 6, 1995, pp. 621–638.

[16] Spangler, C. A., Hilbing, J. H., and Heister, S. D., "Nonlinear Modeling of Jet Atomization in the Wind-Induced Regime," *Physics of Fluids*, Vol. 7, No. 5, pp. 964–971, 1995.

[17] Lamb, H., *Hydrodynamics*, 6th ed., Dover, New York, 1982.

[18] Sterling, A. M., and Sleicher, C. A., "The Instability of Capillary Jets," *Journal of Fluid Mechanics*, Vol. 68, Pt. 3, 1975, pp. 477–495.

[19] Oefelein, J. C., and Yang, V., "Comprehensive Review of Liquid-Propellant Combustion Instabilities in F-1 Engines," *Journal of Propulsion and Power*, Vol. 9, No. 5, 1993, pp. 657–677.

[20] Rutz, M. W., "Effect of Transverse Acoustic Oscillations on Behavior of a Liquid Jet," M.S. Thesis, Purdue Univ., School of Aeronautics and Astronautics, West Lafayette, IN, 1995.

[21] Rutland, D. F., and Jameson, G. J., "A Non-Linear Effect in the Capillary Instability of Liquid Jets," *Journal of Fluid Mechanics*, Vol. 46, Pt. 2, 1971, pp. 267–271.

[22] Lafrance, P., "Nonlinear Breakup of a Laminar Liquid Jet," *The Physics of Fluids*, Vol. 18, No. 4, 1975, pp. 428–432.

[23] Dressler, J. L., "Two Dimensional, High Flow, Precisely Controlled Monodisperse Drop Source," Wright Lab., WL-TR-93-2049, Wright–Patterson AFB, OH, 1993.